Impact of spin state transition on vibrations of [Fe–(PM-BiA) 2(NCS)2] and [Fe –(PM-PEA)2(NCS)2] spin crossover compounds: experimental and theoretical far IR and Raman study

Amine Ould-Hamouda, Benjamin Viquerat, Jérôme Degert, Samir Matar, Jean François Létard, François Guillaume, Eric Freysz

Impact of spin state transition on vibrations of [Fe–(PM-BiA)$_2$ (NCS)$_2$] and [Fe –(PM-PEA)$_2$ (NCS)$_2$] spin crossover compounds: experimental and theoretical far IR and Raman study.

Amine Ould-Hamouda,[a] Benjamin Viquerat,[a] Jérôme. Degert,[a] Samir F. Matar,[b,d] Jean François Létard, François Guillaume,[c] and Eric Freysz*[a]

Abstract: Far IR and Raman spectroscopy of [Fe–(PM-BiA)$_2$ (NCS)$_2$] and [Fe –(PM-PEA)$_2$ (NCS)$_2$] are performed to record the vibration modes of these complexes and their evolutions during spin state transition. THz spectroscopy is used to measure the far IR absorption of these compounds down to 20 cm^{-1}. Using density functional theory calculations we are able to retrieve and to visualize these vibrations in both high spin and low spin states. In both compounds, Raman spectra recorded in the 800 cm^{-1} 2250 cm^{-1} wavenumber range are well accounted for by our computations. For far IR vibration modes, most of the experimental absorption peaks above 100 cm^{-1} are well reproduced. However, below 100 cm^{-1}, marked differences are recorded. For [Fe–(PM-BiA)$_2$ (NCS)$_2$] we demonstrate that the interactions with surrounding molecules impacts non-negligibly the computed far IR spectra and can partly correct for this difference.

Introduction

Iron (II) transition metal complexes can undergo spin crossover (SCO) from low spin (LS, S=0) to high spin (HS, S=2) state.[1] During this transition the complexes record important modifications that affect many of their properties.[2] The structural reorganization of the ligands around the metal center gives rise to an energy barrier between the LS and HS state and shifts the d-d metal and metal-ligand absorption bands.[3] One of the fascinating phenomena discovered and mainly recorded at very low temperature in SCO complexes is the possibility to photoswitch back and forth the complexes between the LS and HS state.[3–5] This phenomenon is called light-induced excited spin state trapping (LIESST) and reverse-LIESST. It has been shown that the stability in temperature of the LIESST effect strongly depends on the energy barriers between the LS and HS state as well as on the tunnel effect between the energy barriers.[6] At very low temperature, the relaxation process between the HS→LS relaxation follows the non adiabatic multi-photon theory. At more elevated temperature, the relaxation process is thermally activated and can be regarded as a tunneling from thermally populated vibration levels of the HS state.[7] In fact the driving force governing the temperature induced SCO phenomenon is the increase in entropy upon LS to HS transition. It was stressed that in the [Fe(phen)$_2$(NCS)$_2$] molecular complex vibrations have the larger contribution (ca. 70%) to the entropy change accompanying SCO.[8] Since the SCO is always accompanied by important changes in the coordination environment of the transition metal, it was considered that the predominant contribution should arise from the metal-ligand stretching. Indeed a relatively elementary picture, confirmed by quantum chemistry calculations, indicates that the shorter metal-ligand distances of the LS state should lead to a higher iron-ligand binding energy and therefore to higher metal-ligand stretching frequencies compared to the HS state. Different models accounting for the role of vibrations based on Debye model have been proposed.[9–14] For the SCO complex [Fe(phen)$_2$(NCS)$_2$] an evaluation of the vibrational contribution to entropy based on consideration of the 15 distortion modes alone of an idealized FeN_6 octahedron has been performed.[15] But the vibration spectrum of this SCO complex is rather complex and 147 normal modes have to be considered. To overcome this limitation, density functional theory (DFT) computations have been performed on [Fe(phen)$_2$(NCS)$_2$] SCO complex.[16] These computations provide an interesting means for a full assignment of vibrational modes, which as indicated by different reviewers, may definitely help a deeper understanding of the SCO phenomena. The DFT computations performed for the SCO complex [Fe(phen)$_2$(NCS)$_2$] were also compared to measurement performed by IR and Raman spectroscopy and nuclear inelastic scattering (NIS).[17] NIS is an interesting technique that makes it possible to extract the frequencies of normal modes that involve significant mean-square displacement of the metal center.[18,19] The comparison between experiment and theory clearly evidences that only the low energy vibrational are markedly affected. However, such comparisons between DFT computations and experiments are quite scarce in the literature.[17–20] In the context of the development of ultrafast time resolved spectroscopy, the demand for such studies has been renewed. Indeed, it is well known that iron(II) SCO molecules in solution or SCO-molecular crystals can undergo an ultrafast photo-switching between LS and HS states.[21–24] Indeed it has been shown that an ultrashort laser pulse brings the complexes in an excited HS state which within less than 100 fs relaxes through intersystem crossing to the HS state.[25] During this process most of the electronic energy is damped through specific vibration modes.[23,24] Hence, in order to spot the vibration relaxation channels of photo-excited SCO complexes, it is important to identify these vibrations and their possible coupling with lattice vibration (i.e. phonons). In this context it is important to further stress that these vibrations at very small frequencies have not been accounted in numerical simulations so far undertaken, the latter being strongly affected by intermolecular interactions.

In the present work, through combining Raman and terahertz time domain spectroscopy (THz-TDS), we have measured the vibration modes of molecular crystals of [Fe(PM-BiA)$_2$(NCS)$_2$], and [Fe(PM-PEA)$_2$(NCS)$_2$] spin crossover complexes in both the LS and HS states.

[a] Amine Ould-Hamouda, Benjamin Viquerat, Jérôme Degert and Eric Freysz,, Universite Bordeaux, CNRS UMR 5798, LOMA, 358 cours de la libération, 33405 Talence Cedex, France
E-mail: eric.freysz@u-bordeaux.fr
[b] Samir Matar and Jean François Létard, CNRS, Unversite Bordeaux, ICMCB, F 33400 Talence, France
[c] François Guillaume, Université Bordeaux, CNRS, ISM, F 33405 Talence Cedex, France
[d] Samir Matar, Lebanese German University, LGU, Sahel-Alma Campus, P.O. Box 206 Jounieh Lebanon.

Our paper intends to specifically evidence the impact of the spin state transition on the modification of the low vibration modes rather than computing the entropy change. Hence to identify the modes active in the far Infra-Red (IR), we use THz-TDS spectroscopy. The latter technique is a very convenient mean to study the IR absorption spectra of low vibration wavenumbers ($\bar{\nu} \leq 200\ cm^{-1}$) that are usually more difficult to explore with conventional IR spectroscopy tools. Knowing the crystalline arrangement of the studied material, these THz and Raman spectra are compared with spectra computed using quantum molecular chemistry in the frame of DFT. In the 100 cm^{-1}–2400 cm^{-1} spectral window, the experimental and computed Raman spectra are in good agreement, indicating the ability of DFT to account for vibration modifications induced by a SCO process in these complexes. For far-IR absorption, experimental and theoretical positions of the IR absorption peaks are rather good above 100 cm^{-1}. Below 100 cm^{-1}, we show that the interactions of such complex with its neighboring ligands modify the position of the IR absorption peaks below 100 cm^{-1} and affect the IR oscillator strength. This reveals the subtle interactions of the SCO complexes within their crystalline structures.

Experimental results

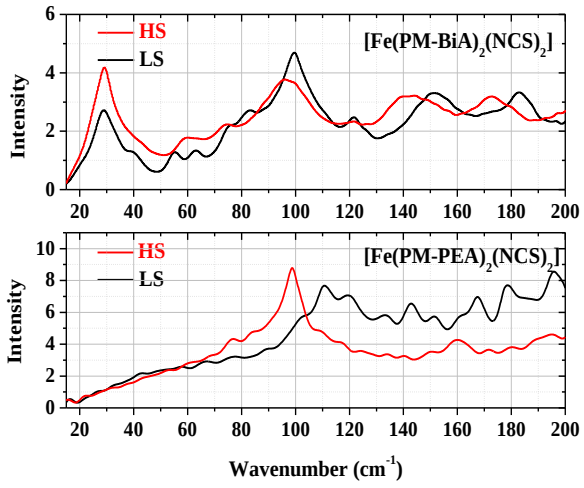

Figure 1 THz-TDS spectra of the $[Fe(PM–L)_2(NCS)_2]$ micro-crystals

TDS-THz spectroscopy of $[Fe(PM\text{-}L)_2(NCS)_2]$ microcrystals, where L=BiA or PEA, were done as follows. The powder of microcrystals was deposited on a thin plate of high density polyethylene over which a small layer of vacuum grease was spread. The latter ensures that the micro-crystals are properly sticking to the PEHD plate. The reference THz spectrum was measured using the PEHD plate over which the vacuum grease was deposited. The absorption of the vacuum grease in the THz range was found to be weak. A cryojet (Oxford) was used to bring the temperature below or above the LS to HS spin state transition temperature

The THz absorption spectra of $Fe(PM\text{-}L)_2(NCS)_2]$ microcrystals in the LS and HS are displayed in Figure 1. Above 100 cm^{-1} wavenumbers, one can notice marked absorption peaks that shift in position from the LS to HS state. This is at variance with the THz-spectra recorded in $[Fe(NH_2\text{-}trz)_3]^{2+}$ spin SCO polymers. The latter have broader absorption peaks ($\Delta\nu \approx 1$ THz) in the THz spectral range.[26] As expected and thanks to the good crystalline structure of SCO micro-crystals, the absorption peaks are narrower ($\Delta\nu \approx 1$ THz). It is interesting to notice that the IR absorption peaks of both compounds present marked differences both in position and amplitude.

Using conventional FTIR measurements, M. Hoeffer has also measured the IR spectra of these compounds within the 100 cm^{-1} (~3 THz) -700 cm^{-1} (~21 THz) frequency range.[27] In the frequency region where we can compare our measurements a good agreement is found. However, one should notice that THz-TDS spectroscopy is more suited for the range of low wavenumbers (<200 cm^{-1}) whereas FTIR gives more easily access to the range of higher wavenumbers (>100 cm^{-1}).

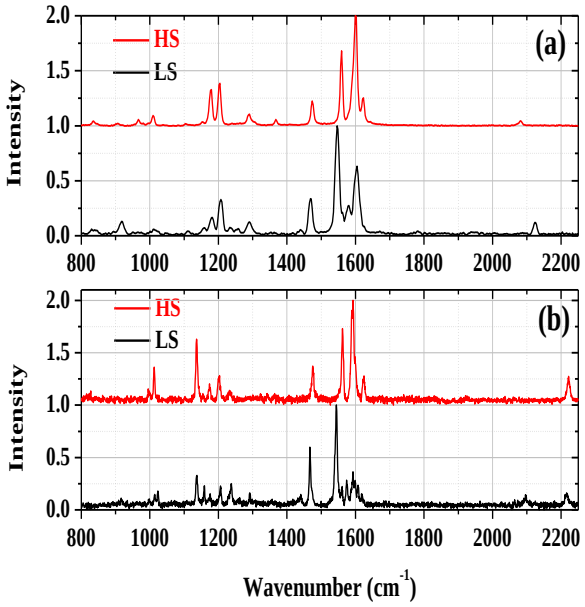

Figure 2: Raman Spectra of of (a) $[Fe(PM–BiA)_2(NCS)_2]$ and (b) $[Fe(PM\text{-}PEA)_2(NCS)_2]$.

The Raman spectra of the $[Fe(PM–L)_2(NCS)_2]$ micro-crystals in the LS and HS states are displayed in Figure 2. As reported previously, the LS to HS transition induces marked changes in the Raman spectra of the powders of micro-crystallites. Many Raman peaks appear or disappear when the spin state transition takes place

Numerical computation results

To complete the computation we called for DFT theoretical models (B3LYP type) that provide the best results for the calculation of the spin state splitting.[28,29] Also beside B3LYP hybrid functional (defined in short hand as a mixture of HF-like exact exchange plus FT-like correlation) , we used modified 'tunable' one as well, commonly known as B3LYP* (weighting differently the afore mentioned mixture). This worked accurately upon using a large and complete enough basis set mainly all electrons "6-311g(*d,p*)". Also ECP (effective core potential) basis sets as LANL2DZ were used for reducing computational cost for such large complex molecular systems and to circumvent having to describe relativistic effects in deep core electrons. Nevertheless results with calculations based on all electrons basis sets were preferred and achieved accurately thanks to massively parallel G09 calculations (Linda).

The IR and Raman active modes of the molecular complexes have been computed knowing the molecular arrangement of the complex thanks to X-ray diffraction.

A. The isolated [Fe(PM-BiA)2(NCS)2]complex

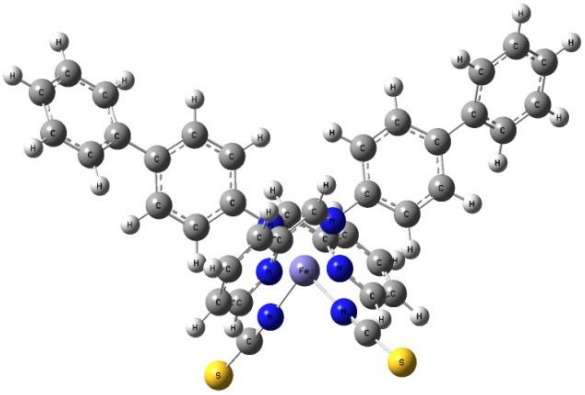

Figure. 3: Molecular structure of the $[Fe(PM\text{-}BiA)_2(NCS)_2]$ complex in the LS state considered for the computations. Iron, carbon, nitrogen, sulfur, hydrogen atoms are depicted in violet, grey, blue, yellow and light grey, respectively.

Figure 3 displays the arrangement of the molecular complex in the LS state we considered for the computation. After optimization of the structures in the LS and HS states, we noticed that the spin transition results in the change of the metal-ligand bond length of Δr=0.266/0.285 Å for (PM-BiA) and 0.1 Å for NCS. The angle between the Fe^{II} and the two NCS ligands increases from 93° to 103°. The large entropy variation (~ 59 J mol^{-1} K^{-1}) deduced from heat capacity measurements during the transition reflects this large difference between the two spin states.[30] This important metal-ligand bond length change should result in marked change in the IR absorption and Raman spectra.

Besides variation of the C-N stretching mode at 2100 cm^{-1}, significant changes are also expected in the α-dimiine stretching region lying in between 1500-1700 cm^{-1}.

B. Isolated $[Fe(PM\text{-}PEA)_2(NCS)_2]$complex

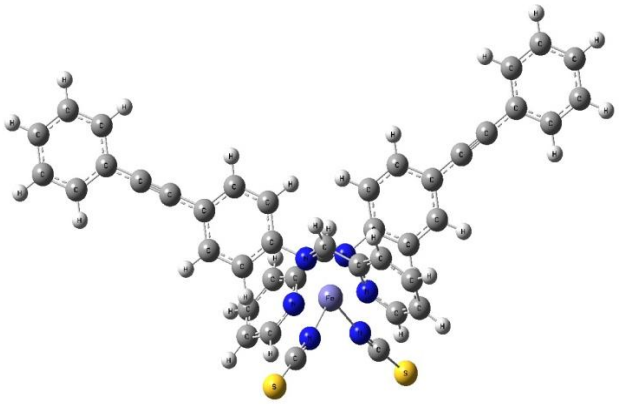

Figure 4 Molecular structure of the $[Fe(PM\text{-}PEA)_2(NCS)_2]$ complex in the LS state considered for the computations. Iron, carbon, nitrogen, Sulfur, hydrogen atoms are depicted in violet, grey, blue, yellow and light grey, respectively.

The arrangement of the complex in the LS state we consider for this computation is displayed in Figure 4. For the $[Fe(PM\text{-}PEA)_2(NCS)_2]$ complex, the spin transition results in the change of the metal-ligand bond length of Δr=0.192/0.151 Å for (PM-PEA) and 0.05 Å for NCS. The angle between the Fe^{II} and the two NCS ligands increases from 94° to 115°. As the temperature of the crystal is increased from 140 K to room temperature, the rearrangement of the molecular complexes is accompanied by a structural phase transition from the orthorhombic *Pccn* space group to the monoclinic $P2_1/c$ space group. It is noteworthy that compared to $[Fe(PM\text{-}BiA)_2(NCS)_2]$ complexes, the transition from the LS to HS state results in a smaller increase of the metal-ligand bond length that is compensated by a larger angle of the NCS-Fe^{II}-NCS. This lesser increase of metal-ligand bond length should result in smaller change of the C-N stretching frequency. For instance, we may expect smaller variations of the C-N stretching mode at 2100 cm^{-1} but, as the vibration of the α-diimine should be hindered by the increase of the NCS-Fe^{II} angle, more drastic changes should be recorded in the α-diimine stretching region.

Discussion and comparison of experimental and computed IR and Raman spectra.

A. The isolated $[Fe(PM\text{-}BiA)_2(NCS)_2]$ complex

The IR and the Raman spectra that we computed in the region of interest and in the LS and HS states are displayed in Figure 5. One should stress that large evolutions of the absorption are also recorded in the 20 cm^{-1}-200 cm^{-1} wavenumbers range. This clearly indicates that the LS to HS spin transition affects a large number of IR and Raman active modes.

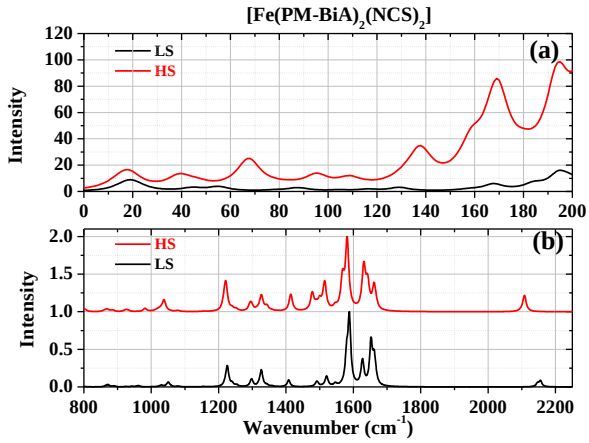

Figure 5: Computed IR (a) and Raman (b) spectra of the $[Fe(PM\text{-}BiA)_2(NCS)_2$ complex.

As displayed in Figure 6, in this compound, the agreement between computed and measured Raman peaks in the high wavenumber region is quite good in both the HS and LS states. To compare more accurately these data we applied the wavenumber scaling factor 0.967 that correct for the approximation made in the computation using the hybrid functional "B3LYP" as well as a modified 'tunable' one, B3LYP* provided a large and complete enough basis set such as all electrons "6-311g(*d*,*p*)" and/or effective core LANL2DZ (*Los Alamos National Laboratory with Double Zeta* polarization). The use of different sets of all electrons basis sets did explain the observed differences. Also with respect to "6-311g(*d*,*p*)", testing with lower basis set 6-31g(*d*,*p*) led to less accurate results on one hand and with higher basis set: 6-311++g(*d*,*p*) (++ = diffuse functions) did not change results significantly on the other hand.

When both the experimental and computed Raman spectra are normalized, the amplitude and the position of the Raman peaks are found to agree very well. However, some peaks have higher amplitudes in the experimental data.

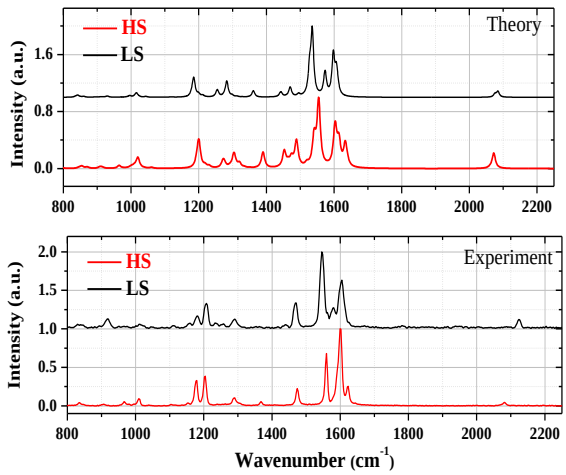

Figure 6 : Comparison of the normalized experimental and computed Raman spectra of the [Fe(PM-BiA)2(NCS)2] complex.

We have reported in Table 1 the calculated and experimental Raman bands of the $[Fe(PM\text{-}BiA)_2(NCS)_2]$ complex in the LS and HS states and the proposed vibrational mode assignments. The positions of most of the experimental Raman peaks agree well with the computed ones.

	LS		HS		Assignment
	Exp.	*Cal.*	*Exp.*	*Cal.*	
1	2123	2064	2084	2024	$\nu_{NCS}(CN)$
2	1607	1595	1619	1594	$\nu_{r3}(CC)+\delta_{r3}(HCC+CCC)$
3	1584	1586	1603	1577	$\nu_{r1}(CC)+\delta_{r1}(HCC+CCC)$
4	1545	1524	1558	1569	$\nu_{r1}(CC)+\delta_{r1}(HCC)+\nu_{im}(CN)$
5			1545	1504	$\nu_{im}(CN)+\delta_{r1}(HCC)+\delta_{r2}(HCC)+\delta_{r3}(HCC)$
6	1470	1460	1471	1454	$\nu_{r1}(CC+CN)+\delta_{r1}(HCC+HCN)$
7	1439	1435			$\nu_{r1}(CN)+\delta_{r1}(HCC+HCN)$
8			1367	1419	$\delta_{r1}(HCC+HCN)$
9	1290	1352	1290	1357	$\delta_{im}(HCN)+\delta_{r1}(HCC)$
10	1206	1274	1206	1274	$\nu_{r2\text{-}r3}(CC)+\delta_{r2}(HCC)+\delta_{r3}(HCC)$
11	1177	1177	1175	1173	$\delta_{r2}(HCC)+\nu_{r2\text{-}im}(CN)$
12			1152	1166	$\delta_{r1}(HCC)$
13	1015	1009	1006	996	$\delta_{r1}(HCC+HCN)+\nu_{r1}(CC)$
14			968	943	$\tau_{r1\text{-}im}(HCCN)$
15	923	924	910	889	τ_{r1} (HCCH)+$\tau_{r2\text{-}im}$(HCNC)

Table 1: Experimental (Exp.) and calculated (Ca.) Raman bands (cm^{-1}) and their assignments in terms of normal coordinates for $[Fe^{II}(PM\text{-}BiA)_2(NCS)_2]$ complex in LS and HS phases. The subscripts of the symbols refer to the PM-BiA ligand functional groups defined in Fig. 7. Meaning of symbols: ν, stretching; δ, deformation; τ, torsion. The labels in the left column refer to the movie files describing the vibrations that are reported in the supplementary material.

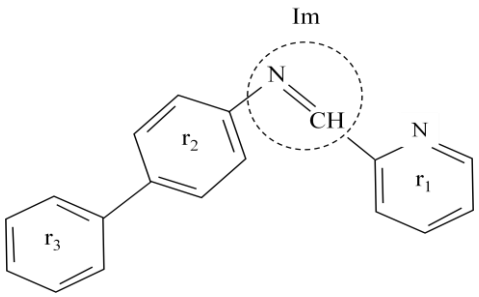

Figure 7: Schematic representation of the PM-BiA ligand and the notations used to identify the functional groups in Table 1.

The experimental and computed IR spectra of the $[Fe(PM\text{-}BiA)_2(NCS)_2]$ complex are displayed in Figure 8. Here again to compare more accurately these data we applied the wavenumber scaling factor 0.967 that corrects for the approximation made in the computation. Prior to the discussion, we have to underline that the amplitude of the IR modes in the spectral region scanned by the THz-TDS spectroscopy is weak. The amplitudes of the computed IR active modes are also weak. Therefore, we have to stress that comparison between experiment and theory in this spectral range is difficult. In the LS state, the four main experimental peaks around 215 cm^{-1}, 185 cm^{-1}, 150 cm^{-1}, 100 cm^{-1} and 30 cm^{-1} may be related to the theoretical IR absorption peaks centered around 215 cm^{-1}, 195 cm^{-1}, 168 cm^{-1}, 90 cm^{-1} and 20 cm^{-1}. At maximum, the wavenumber shift between experiment and theory is about 15±5 cm^{-1}. One should also notice an important difference in the oscillation strength of these modes. In the HS state the same behavior is recorded the five experimental peaks centered at about 30 cm^{-1}, 95 cm^{-1} 140 cm^{-1}, 175 cm^{-1} and 195 cm^{-1} have a counterpart in the computed spectra centered at about 40 cm^{-1}, 95 cm^{-1}, 140 cm^{-1}, 170 cm^{-1} and 195 cm^{-1}. It is worth to mention that as indicated by the arrows in Figure 8 most of the theoretical absorption peaks can be related with minor shifts to an experimental absorption peak. Moreover in the HS state the complexes are less rigid and a down wavenumber shift is always observed when this compounds switches from the LS to the HS state.

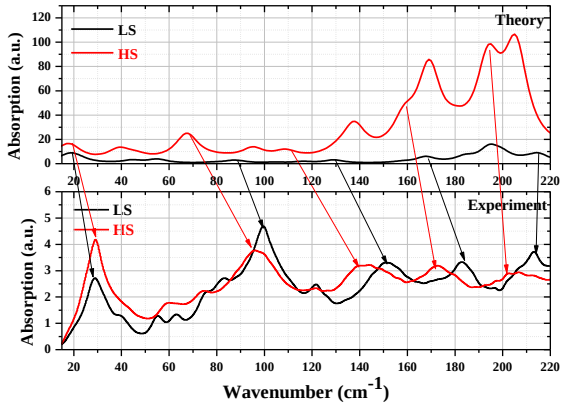

Figure 8: Comparison of the normalized experimental and computed IR spectra of the $[Fe(PM\text{-}BiA)_2(NCS)_2]$ complex.

B. The isolated $[Fe(PM\text{-}PEA)_2(NCS)_2]$ complex

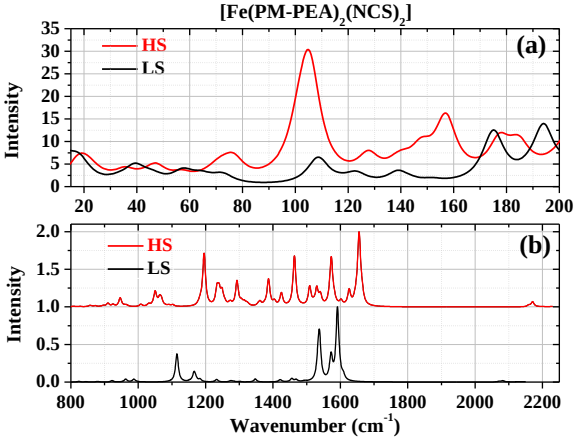

Figure 9: Computed IR (a) and Raman (b) spectrum of the $[Fe(PM\text{-}PEA)_2(NCS)_2]$ complex.

The IR and the Raman spectra computed in the LS and HS states, displayed in Fig. 9, are in agreement with the analysis we proposed previously indicating more drastic changes should be recorded in the α-diimine stretching region during the HS to LS state switching.
The normalized experimental and computed Raman spectra of this compound are displayed in Figure 10. Due to the higher absorption of this compound at the used excitation wavelength, very low laser power was used (<80 µW) so that the experimental spectra are noisier in the low wavenumber regions where the background subtraction procedure is biasing the experimental data. For this compound, one can notice that the agreement between experiment and theory is less accurate when the normalized Raman spectra are compared.

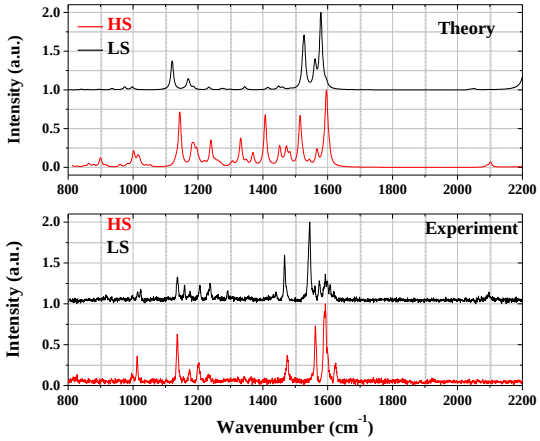

Figure 10 Comparison of the experimental and computed Raman spectra of the $[Fe(PM\text{-}PEA)_2(NCS)_2]$ complex..

	LS		HS		Assignment[a]
	Exp.	*Cal.*	*Exp.*	*Cal.*	
1	2220	2259	2216	2284	$\nu_{Acty}(CC)$
2	2099	2089			$\nu_{NCS}(CN)$
3	1610	1625	1623	1602	$\nu_{r1}(CC)+\nu_{r2}(CC)+\nu_{r3}(CC)+\nu_{Im}(CN)$
4	1600	1615	1600	1595	$\nu_{r1}(CC)+\nu_{r2}(CC)+\nu_{r3}(CC)+\nu_{Im}(CN)$
5			1594	1592	$\nu_{r1}(CC)+\nu_{r2}(CC)+\nu_{Im}(CN)$
6	1594	1608	1589	1585	$\nu_{r1}(CC)+\nu_{r2}(CC)+\nu_{r3}(CC)$
7	1576	1588	1562	1564	$\nu_{r1}(CC+CN)+\nu_{Im}(CN)$
8	1545	1552	1476	1541	$\nu_{r1}(CC+CN)+\nu_{Im}(CN)$
9	1469	1488			$\delta_{r2}(HCC)+\delta_{r3}(HCC)$
10	1441	1475			$\nu_{r1}(CN)+\delta_{r1(}HCC+HCN)$
11			1367	1405	$\delta_{r1(}HCC)+\delta_{Im}(HCN)$
12	1415	1441			$\delta_{r1(}HCC)$
13			1310	1329	$\delta_{r1(}HCC)+\nu_{Im}(CN)$
14	1357	1370	1203	1238	$\delta_{Im}(HCN)$
15	1293	1296			$\nu_{r1}(CN+CC)+\delta_{Im}(HCN)$
16			1175	1180	$\delta_{r2}(CCC+HCC)$
17	1262	1257			$\delta_{r1(}HCC)+\delta_{Im}(HCN)$
18	1238	1209			$\delta_{r2}(HCC+CCC)$
19	1208	1196			$\delta_{r3}(HCC)$
20	1177	1192			$\delta_{r1}(HCC)$
21	1160	1178			$\delta_{r1}(HCC)$
22	1138	1141	1137	1142	$\nu_{r2\text{-}Acty}(CC)+\nu_{r3\text{-}Acty}(CC)+\delta_{r2}(HCC)+\delta_{r3}(HCC)$
23			1013	1018	$\delta_{r1}(CCC+CCN)$
24			1000	1000	$\delta_{r1}(CCC+CCN)$
25	1024	1016			$\delta_{r1}(CCC+CCN)$
26	1013	992			$\delta_{r3}(CCC)$
27	999	953	961	958	$\gamma_{Im}(CH)$

Table 2: Experimental (Exp.) and calculated (Ca.) Raman bands (cm^{-1}) and their assignments in terms of normal coordinates for $[Fe^{II}(PM\text{-}PEA)_2(NCS)_2]$ complex in LS and HS phases. The subscripts of the symbols refer to the PM-PEA ligand functional groups defined in Fig. 11. Meaning of symbols: ν, stretching; δ, deformation; τ, torsion; γ out of plane bending. The labels in the left column refer to the movie files reported in the supplementary material that are describing the vibrations.

In Table 2, we have reported the computed and experimental Raman bands displayed in figure 11 and assigned the different Raman modes in terms of internal coordinates for this complex. One can conclude that even if their amplitudes differ, the positions of most of the experimental Raman peaks agree well with the computed ones.

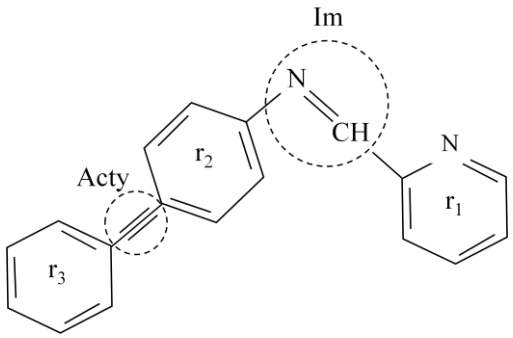

Figure 11: Schematic representation of the PM-PEA ligand and the notations used to identify the functional groups in Table 2.

The measured and computed IR spectra of the $[Fe(PM\text{-}PEA)_2(NCS)_2]$ complex are displayed in figure 12. Once we applied the wavenumber scaling factor 0.967 that corrects for the approximation made in the computation, a good agreement between the computed and experimental spectra is found. Here we should emphasize that the amplitudes of the peaks are higher compared to the $Fe(PM\text{-}BiA)_2(NCS)_2]$ and the spectral changes recorded above 100 cm^{-1} wavenumber in this compound are more drastic, making a comparison between computations and experiments simpler. One can notice that above 100 cm^{-1}; most of the peaks found in the experimental data have correspondence counterpart in the theoretical spectra.

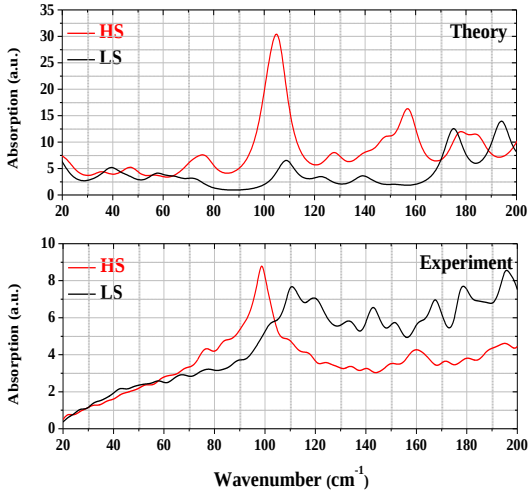

Figure 12: Comparison of the experimental and computed low wavenumber IR spectra of the $[Fe(PM\text{-}PEA)_2(NCS)_2]$ complex.

In this compound in the HS state, the most intense peak centered at about 100 cm^{-1} is found in both the computed and experimental IR spectra. The two other weaker absorption peaks centered at 75 cm^{-1} and

140 cm^{-1} in the theoretical spectra have their experimental correspondence. As the complex is switched from the HS to the LS state, the computed spectra indicates that the amplitude of the main absorption peak centered at 100 cm^{-1} is reduced and its position is shifted to higher wavenumber. Other peaks centered at 175 cm^{-1} and 195 cm^{-1} appears. This trend is clearly found in the experimental spectra indicating that the computation is indeed able to grasp the main trends found in far-IR spectra.

C. The *[Fe(PM-PEA)$_2$(NCS)$_2$]* complex in interaction with it neighborhood

Even if the computations we performed assume that the complex has the optimized structure, one may wonder on the impact of the neighboring complexes on the THz spectra especially in the low frequency region where interactions between the complexes as well as the vibrations of the lattice should respectively modify and contribute to the low frequency part of the IR spectrum. In order to roughly evaluate the impact of the neighboring molecules on the hindrance of some vibrations of the complex, we have introduced the two neighboring BiA ligands in the computation, whose positions are defined according to X-ray diffraction. The cluster we used to perform this computation is displayed in Fig. 13. Even if such approximation is rather crude, its impacts on the computed THz spectra may be quite instructive, indicating whether such a consideration is meaningful. The results of the computation of far-IR absorption performed considering the [Fe(PM-BiA)$_2$(NCS)$_2$] complex in both the LS and HS states is displayed in Figure 14. Comparison of experimental and computed data reveals that introduction of the two BiA ligands non-negligibly impacts the far-IR absorption of the complex. In both the LS and HS states one can notice the increase of the normalized absorption in far-IR lattice vibration below 160 cm^{-1} and the decrease of the absorption above 160 cm^{-1}. Comparison of the IR spectra of the complex computed with and without the two ligand molecules also indicates that below 100 cm^{-1} the amplitudes as well as the positions of the peaks are affected. The change of the amplitude is probably related to the change of the local symmetry of the complex with or without the two added BiA ligands, whereas the change of the central wavenumber of the absorption peak is likely related to the modification of the low frequency modes of the complex by the two added BiA.

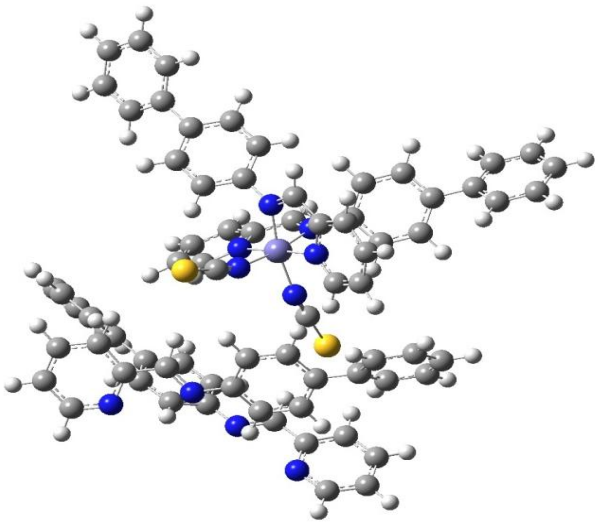

Figure 13: [Fe(PM-BiA)$_2$(NCS)$_2$] complex in interaction with its two neighboring BiA ligands. (central) Iron, carbon, nitrogen, sulfur, hydrogen atoms are depicted in violet, grey, blue, yellow and light grey, respectively.

Even if, for both the HS and LS states, the experimental and computed IR absorption spectra are in better agreement some discrepancies remain. In fact, we cannot neglect the lattice vibrations at low frequencies. The latter should also impact IR and Raman active mode but such more complex computations are beyond of the scope of this work.

We have also tried to perform similar computations for the [Fe(PM-PEA)$_2$(NCS)$_2$] complex. For this complex the numerical convergence was not satisfactory. However, as we already mentioned for the [Fe(PM-BiA)$_2$(NCS)$_2$] complex, we expect that the introduction of the two PEA ligands will impact the position of the IR absorption peaks below 100 cm^{-1}. Luckily for this complex, we did not record marked absorption peaks below this wavenumber. Hence, the introduction of the two PEA ligands should not drastically change the LS and HS IR absorption spectra of this compound.

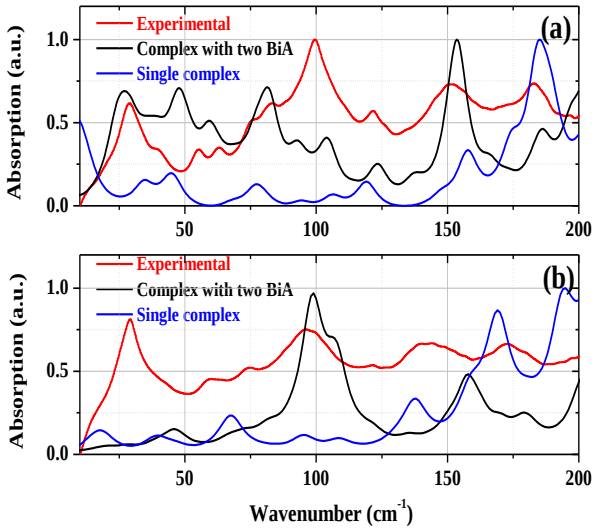

Figure 14: Comparison of the normalized IR spectra of the [Fe(PM-BiA)$_2$(NCS)$_2$] complex in the LS (a) and HS (b) state computed with (black line) and without (blue line) the two neighboring BiA ligands with the experimental data (red line)

Conclusions

The spin state transition recorded in different [Fe–(PM-L)$_2$ (NCS)$_2$] complexes with L=BiA or PEA indicates that marked spectral changes can be recorded in both Raman and IR active modes in mid and THz (i.e. far-IR) spectral ranges. The experimental spectra are found to agree well with the computed ones using quantum molecular chemistry in the framework of density functional theory. For the Raman spectra, we have shown that depending on the studied complex the spin transition affects differently the C-N and α-diimine stretching modes. The latter mode results from an increase of the NCS-Fe angle. For far-IR absorption spectroscopy, our data clearly indicate that the neighboring ligands and lattice vibrations of the molecular crystal affect the IR absorption of complexes. The latter illustrates how local as well as long range arrangements of SCO complexes may impacts vibrations of these complexes

Experimental Section

A. Samples

The synthesis of the samples was performed with usual techniques without any special care to exclude oxygen or moisture. Nevertheless, solvents were used freshly distilled, methanol over Mg and CH_2Cl_2

over CaH_2. The $[Fe(PM\text{-}BiA)_2(NCS)_2]$ micro-crystals were synthesized using the previously reported procedure.[30] Change of the synthetic conditions makes it possible to obtain powder sample with gradual (phase II) or abrupt (phase I) spin transitions. The measurements reported hereafter were performed with phase I micro-crystallites. Phase I crystallizes in orthorhombic space group Pccn. The crystal structure was determined both at 298 K in the HS state (a=12.949 (5) Å, b= 15.183(2) Å, c=17.609(5) Å, V=3464(2) $Å^3$) and at 140 K in the LS state (a=12.370 (3) Å, b= 14.764(3) Å, c=12.28(4) Å, V=3338(2) $Å^3$). The spin state transition takes place without change of the crystallographic space group. This material has been shown to give rise to a small hysteresis of 168-173 K.

The synthesis of $[Fe(PM\text{-}PEA)_2(NCS)_2]$ has also been described in the literature.[31] The sample we studied was synthesized according to the procedure previously reported. The crystal is monoclinic P21/c at 293 K and orthorhombic *Pccn* at 140 K. The crystal structure was determined both at 298 K in the HS state (a=15.637 (1) Å, b= 14.566(8) Å, c=16.821(13) Å, V=3826(4) $Å^3$) and at 140 K in the LS state (a=14.357(7) Å, b= 14.291(6) Å, c=17.448(13) Å, V=3580(4) $Å^3$). The spin state transition takes place with a quite severe crystallographic phase transition from monoclinic to orthorhombic. This material has been shown to give rise to a very large hysteresis of 37-60 K and it shows a weak LIESST effect.

B. Set-up for THz and Raman spectroscopy

The set-up used to perform THz-TDS has been described elsewhere.[32] In short, a THz beam consisting in a single-cycle THz wave is generated ionizing air using the fundamental and the second harmonic of 50 fs pulses centered at λ=800 nm. After transmission through the sample, this wave is measured by electro-optical (EO) sampling in a 200 µm-thick <110> GaP crystal. This THz detection system records the temporal profile of the electric field of the THz pulses which makes it possible to recover the complex index of refraction of the studied sample on a 0.3–7 THz frequency range. However this method implies to perform two measurements. We first record a reference waveform $E_R(t)$ without the sample and then a signal waveform $E_S^{LS,HS}$ with the sample in the LS and HS state, respectively. The Fourier components of the two signals are obtained through a Fourier transform and define the complex transmission function of the sample. The latter is directly related to the complex refractive index of the sample. The frequency-dependent complex dielectric constant of the sample is obtained by computing the complex ratio of the output amplitude spectrum to the input of the reference spectrum. This makes it possible to retrieve the absorption spectrum of the sample in the LS and HS states.[32,33] The THz spectra were collected in the LS state at T=100 K and at T=293 K in the HS state.

Raman spectra were collected in backscattering geometry using an excitation line centered at 785 nm and a LabRam HR-Evolution spectrometer (Horiba Jobin-Yvon) with 2 cm^{-1} spectral resolution. The spectrometer was coupled to an Olympus microscope with an ultra long working distance 50 X Plan objective (numerical aperture NA=0.55). A Linkam THS 600 stage positioned under the microscope objective was used to perform the heating and cooling cycles with a rate of 2 K per minute. Once the set temperature was reached, the sample was maintained at this temperature for 5 min for thermal equilibration before exposing it to the laser beam. The sample was initially warmed at 400 K in an atmosphere of dry N_2 to eliminate water. The sample was subsequently held in dry N_2 at atmospheric pressure during all experiments. The laser power at the output of the microscope objective was systematically measured prior to measurements and could be tuned using density filters that attenuate the laser intensity. Due to the high absorption of our samples, the signal to noise ratio of the Raman spectra was poor below 750 cm^{-1}. The latter absorption may give rise to pre-resonant features modifying the amplitude of the Raman peaks which are not accounted for by the DFT computations. The Raman spectra were collected in the LS state at T=100 K and at T=293 K in the HS state.

C. Computations

The vibration modes are computed through quantum molecular chemistry. Nowadays, it is becoming well established that Density Functionnal Theory (DFT) framework brings far accurate results regarding the energetic and related properties of molecular complexes than Hartree Fock calculations. Although several computational methods are known for the molecular chemical compounds, we used in our studies the *Gaussian*09 commercial code.[34] The molecular frequencies depend on the second derivative of the energy with respect to the nuclear positions. This implies the use of the proper theoretical framework of calculation to optimize the geometry the molecular complex as a first step. The minimum geometry configuration should be close to the experimental one (volume, distances…) as a validation test before the IR/Raman frequencies calculation. In agreement with the literature, we used the DFT theoretical models (B3LYP type) that provide the best results in this respect

Acknowledgements

The authors acknowledge support through ANR project "OptoMaTS", Conseil Régional d'Aquitaine for funding equipment of the platform "COLA" and the project "MatTS", A.O.H. is grateful to the Conseil Régional d'Aquitaine for financial support. Computation facilities were provided by MCIA-University of Bordeaux center. The Conseil Régional d'Aquitaine and Europe (FEDER program) are also thanked for funding equipment of the Vibrational Spectroscopy and Imaging (SIV) platform at ISM.

[1] P. Gütlich, H. A. Goodwin, Eds. , *Spin Crossover in Transition Metal Compounds I*, Springer Berlin Heidelberg, Berlin, Heidelberg, **2004**.
[2] P. Gütlich, Y. Garcia, Th. Woike, *Coord. Chem. Rev.* **2001**, *219–221*, 839–879.
[3] J.E. Huheey, E.A. Keiter and R.L. Keiter, in *Inorg. Chem. Princ. Struct. React.*, Harper Collins College Publishers, **1993**, pp. 443–447.
[4] S. Decurtins, P. Gutlich, K. M. Hasselbach, A. Hauser, H. Spiering, *Inorg. Chem.* **1985**, *24*, 2174–2178.
[5] A. Hauser, *J. Chem. Phys.* **1991**, *94*, 2741.
[6] A. Hauser, in *Spin Crossover Transit. Met. Compd. II*, Springer Berlin Heidelberg, Berlin, Heidelberg, **2004**, pp. 155–198.
[7] E. Buhks, G. Navon, M. Bixon, J. Jortner, *J. Am. Chem. Soc.* **1980**, *102*, 2918–2923.
[8] M. Sorai, S. Seki, *J. Phys. Chem. Solids* **1974**, *35*, 555–570.
[9] R. Zimmermann, E. König, *J. Phys. Chem. Solids* **1977**, *38*, 779–788.
[10] E. König, in *Complex Chemistry, Structure and Bonding,*, Springer Berlin Heidelberg, Berlin, Heidelberg, **1991**, pp. 51–152.
[11] J. Wajnflasz, *Phys. Status Solidi B* **1970**, *40*, 537–545.
[12] C. Lee, W. Yang, R. G. Parr, *Phys. Rev. B* **1988**, *37*, 785–789.
[13] T. Kambara, *J. Chem. Phys.* **1979**, *70*, 4199.
[14] H. Spiering, E. Meissner, H. Köppen, E. W. Müller, P. Gütlich, *Chem. Phys.* **1982**, *68*, 65–71.
[15] A. Bousseksou, J. J. McGarvey, F. Varret, J. A. Real, J.-P. Tuchagues, A. C. Dennis, M. L. Boillot, *Chem. Phys. Lett.* **2000**, *318*, 409–416.
[16] G. Brehm, M. Reiher, S. Schneider, *J. Phys. Chem. A* **2002**, *106*, 12024–12034.
[17] K. L. Ronayne, H. Paulsen, A. Hoefer, A. C. Dennis, J. A. Wolny, A. I. Chumakov, V. Schünemann, H. Winkler, H. Spiering, A. Bousseksou, et al., *Phys. Chem. Chem. Phys.* **2006**, *8*, 4685.
[18] S. Rat, M. Mikolasek, J. S. Costá, A. I. Chumakov, W. Nicolazzi, G. Molnár, L. Salmon, A. Bousseksou, *Chem. Phys. Lett.* **2016**, *653*, 131–136.
[19] K. Jenni, L. Scherthan, I. Faus, J. Marx, C. Strohm, M. Herlitschke, H.-C. Wille, P. Würtz, V. Schünemann, J. A. Wolny, *Phys Chem Chem Phys* **2017**, *19*, 18880–18889.
[20] J. A. Wolny, R. Diller, V. Schünemann, *Eur. J. Inorg. Chem.* **2012**, *2012*, 2635–2648.
[21] G. Gallé, C. Etrillard, J. Degert, F. Guillaume, J.-F. Létard, E. Freysz, *Appl. Phys. Lett.* **2013**, *102*, 63302.
[22] R. Bertoni, M. Lorenc, A. Tissot, M. Servol, M.-L. Boillot, E. Collet, *Angew. Chem.* **2012**, *124*, 7603–7607.
[23] M. Cammarata, R. Bertoni, M. Lorenc, H. Cailleau, S. Di Matteo, C. Mauriac, S. F. Matar, H. Lemke, M. Chollet, S. Ravy, et al., *Phys. Rev. Lett.* **2014**, *113*, DOI 10.1103/PhysRevLett.113.227402.
[24] G. Auböck, M. Chergui, *Nat. Chem.* **2015**, *7*, 629–633.

[25] J. Tribollet, G. Galle, G. Jonusauskas, D. Deldicque, M. Tondusson, J. F. Letard, E. Freysz, *Chem. Phys. Lett.* **2011**, *513*, 42–47.
[26] B. Viquerat, J. Degert, M. Tondusson, E. Freysz, C. Mauriac, J. F. Létard, *Appl. Phys. Lett.* **2011**, *99*, 61908.
[27] A. Hoeffer, Vibrational spectroscopy on thermally and optically switchable spin crossover compounds, Mainz, **2000**.
[28] M. Reiher, O. Salomon, B. Artur Hess, *Theor. Chem. Acc. Theory Comput. Model. Theor. Chim. Acta* **2001**, *107*, 48–55.
[29] O. Salomon, M. Reiher, B. A. Hess, *J. Chem. Phys.* **2002**, *117*, 4729–4737.
[30] J.-F. Létard, P. Guionneau, L. Rabardel, J. A. K. Howard, A. E. Goeta, D. Chasseau, O. Kahn, *Inorg. Chem.* **1998**, *37*, 4432–4441.
[31] J.-F. Létard, P. Guionneau, E. Codjovi, O. Lavastre, G. Bravic, D. Chasseau, O. Kahn, *J. Am. Chem. Soc.* **1997**, *119*, 10861–10862.
[32] P. Mounaix, N. Lascoux, J. Degert, E. Freysz, A. Kobayashi, N. Daro, J.-F. Létard, *Appl. Phys. Lett.* **2005**, *87*, 244103.
[33] B. Viquerat, J. Degert, M. Tondusson, E. Freysz, C. Mauriac, J. F. Létard, *Appl. Phys. Lett.* **2011**, *99*, 61908.
[34] Gaussian 09, Revision A.02; M. Frisch et al., Gaussian, Inc.: Wallingford, CT, USA, 2009